Electronic and crystallographic structure, hard x-ray photoemission, and mechanical and transport properties of the half-metallic Heusler compound Co_2MnGe

Siham Ouardi, Gerhard H. Fecher,* Benjamin Balke, Andreea Beleanu, Xeniya Kozina, Gregory Stryganyuk, and Claudia Felser
Institut für Anorganische und Analytische Chemie, Johannes Gutenberg Universität, D-55099 Mainz, Germany

Werner Klöß and Hartmut Schrader
Fachbereich Maschinenbau und Kunststofftechnik, Hochschule Darmstadt, D-64295 Darmstadt, Germany

Fabiano Bernardi and Jonder Morais
Instituto de Fisica, Universidade Federal do Rio Grande do Sul, Porto Alegre, RS, Brazil

Eiji Ikenaga
Japan Synchrotron Radiation Research Institute, SPring-8, Hyogo 679-5198, Japan

Yoshiyuki Yamashita, Shigenori Ueda, and Keisuke Kobayashi
NIMS Beamline Station at SPring-8, National Institute for Materials Science, Hyogo 679-5148, Japan
(Received 17 July 2011; revised manuscript received 24 September 2011; published 17 October 2011)

This work reports on the electronic and crystalline structure and the mechanical, magnetic, and transport properties of the polycrystalline Heusler compound Co_2MnGe. The crystalline structure was examined in detail by extended x-ray absorption fine-structure spectroscopy and anomalous x-ray diffraction. The compound exhibits a well-ordered $L2_1$ structure as is typical for Heusler compounds with 2:1:1 stoichiometry. The low-temperature magnetic moment agrees well with the Slater-Pauling rule and indicates a half-metallic ferromagnetic state of the compound, as is predicted by *ab initio* calculations. Transport measurements and hard x-ray photoelectron spectroscopy were performed to explain the electronic structure of the compound. The obtained valence band spectra exhibit small energy shifts that are the result of the photoexcitation process, whereas electron-electron correlation in the ground state is negligible. The vibration and mechanical properties of the compound were calculated. The observed hardness values are consistent to a covalent-like bonding of Co_2MnGe.

DOI: 10.1103/PhysRevB.84.155122 PACS number(s): 61.05.cj, 62.20.−x, 63.20.−e, 71.20.−b

I. INTRODUCTION

Heusler compounds have recently attracted increasing interest, owing to their multifarious properties.[1,2] Research on half-metallic ferromagnetic materials based on Heusler compounds has been rapidly growing since its prediction for NiMnSb in 1983 by de Groot and co-workers.[3] Several Heusler alloys crystallizing in the cubic $L2_1$ structure with space group $Fm\bar{3}m$ (225) have been verified to be half-metallic by electronic band structure calculations.[4] Kübler and co-workers demonstrated that in many Heusler alloys the minority spin density of states (DOS) exhibits a band gap at the Fermi energy while the majority spins are responsible for the metallic properties. Those compounds are considered one of the most useful candidates for tunneling magnetoresistance (TMR) devices, because the magnetoresistance (MR) is expected to be large if the conduction electron spin is 100% polarized. This conduction electron spin can be possibly injected into a semiconductor, when the materials are epitaxially grown on the semiconductor surface.

The Heusler alloy Co_2MnGe, a half-metallic compound, is considered one of the most useful candidates for spintronics since it combines a high Curie temperatures (905 K)[5] and coherent growth on top of semiconductors. Recently, several groups were successful in growing Co_2MnGe epitaxially on semiconductor substrates.[6] Ishikawa and co-workers[7] and Hakamata and co-workers[8] have already fabricated epitaxial magnetic tunnel junctions (MTJs) based on Co_2MnGe and a MgO tunnel barrier, and they found relatively high tunnel magnetoresistance ratios of 185% at 4.2 K and 83% at room temperature with a Co-rich Co_2MnGe film. They have shown that the TMR ratio depends on the amount of Co in Co_2MnGe. Therefore, a systematic study of the influence of the crystal quality on the magnetic and transport properties as well as the half-metallicity in the compounds needs to be made.

The present work reports on a comprehensive theoretical and experimental study of the Heusler compound Co_2MnGe. Electronic structure calculations were carried out to verify and explain its half-metallic ferromagnetic behavior. Anomalous x-ray powder diffraction (aXRD) and extended x-ray absorption fine- structure spectroscopy (EXAFS) were performed for the structure determination and to obtain the cell parameters. To open new fields of application for Heusler compounds, the mechanical and vibrational properties of Co_2MnGe were calculated and the hardness of the compound was experimentally determined. Furthermore, measurements of the magnetic as well as transport properties were performed. To verify the calculated electronic structure a detailed investigation by hard x-ray photoelectron spectroscopy (HAXPES) was carried out.

II. EXPERIMENT

The Co_2MnGe bulk samples were prepared by arc melting of stoichiometric amounts of the constituents in an argon

atmosphere. The arc melting results in polycrystalline ingots. These ingots were annealed in an evacuated quartz tube for 7 d at 800 °C and subsequently for another 7 d at 1000 °C. Directly after annealing, the hot ingots were quenched in ice water. This procedure resulted in samples exhibiting the Heusler type $L2_1$ structure, which was verified by XRD using Mo K_α radiation as well as synchrotron radiation.

The powder diffraction pattern taken with Mo K_α radiation (not shown here) did not exhibit the 002 fcc superstructure reflection, because of the nearly equal scattering amplitudes of the constituent elements, and the intensity of the 111 reflection was extremely low. This complicates the unambiguous determination of the details of the structure. A lattice parameter of about ≈5.75 Å was found from a Rietveld refinement of the low resolution Mo K_α XRD data. Additional high-resolution synchrotron-based scattering experiments (see Sec. III A for details and a improved lattice parameter) have been performed to overcome the problems of structure determination by XRD with Mo K_α radiation.

Anomalous XRD experiments were performed at the x-ray powder diffraction beamline[9] at the bending magnet D10 of the Brazilian Synchrotron Light Laboratory (LNLS). The powder samples were used in complementary EXAFS measurements, which have been performed at the XAFS1 beamline of LNLS[10] using a Si 111 channel-cut monochromator. The spectra were collected at the Co (7709 eV), Mn (6539 eV), and Ge (11103 eV) K edges at room temperature in the transmission mode using three ionization chambers. Standard metal foils were placed at the third chamber to check the monochromator energy calibration.

The magnetic properties of the polycrystalline Co_2MnGe samples were investigated with a superconducting quantum interference device (SQUID, Quantum Design MPMS-XL-5) using small pieces of 23.6 mg. The magnetic moment was determined to be 4.982 μ_B at 5 K (see Fig. 1). Owing to the high Curie temperature of the compound, no noteworthy changes were detected for temperatures up to 300 K.

The transport and specific heat measurements were performed by means of a physical properties measurement system (PPMS; Quantum Design model 6000, supported by LOT, Germany). For transport measurements, sticks of $(2 \times 2 \times 8)$ mm^3 were cut from the ingots. For the specific heat measurements, small sample pieces of approximately 4 mg were used. The temperature was varied from 1.8 K to room temperature. All measurements were performed at a residual pressure of about 9.0×10^{-5} mbar in the chamber.

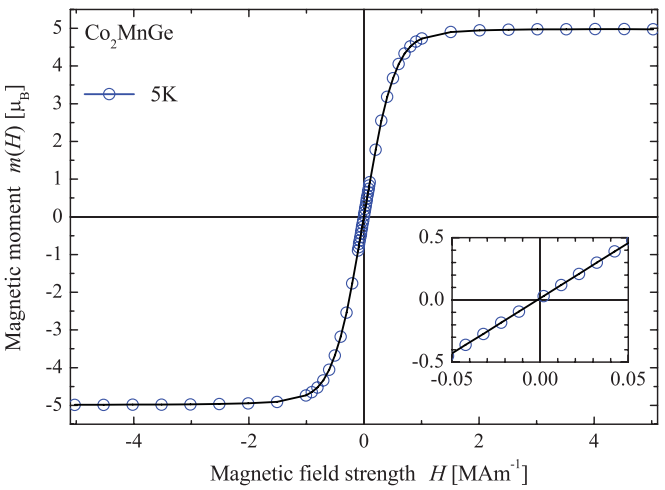

FIG. 1. (Color online) Low-temperature magnetization of Co_2MnGe.

For the HAXPES measurements the sample sticks as used for the transport measurements were fractured *in situ* in the ultrahigh vacuum (UHV) chamber before each measurement to avoid contamination when exposed to air. The HAXPES experiments were performed at the beamlines BL15XU[11] and BL47XU of SPring-8. At BL15XU, the photon energy was fixed at 5.9534 keV using a Si 111 double crystal monochromator and the 333 reflection of a Si channel-cut post monochromator. At BL47XU, the photon energy was fixed at 7.9392 keV using a Si 111 double crystal monochromator and the 444 reflection of a Si channel-cut post monochromator. At both beamlines, the photoelectrons were analyzed and detected by means of hemispherical analyzers (VG Scienta R4000). The overall energy resolution (monochromator plus analyzer) was set to 240 meV, as verified by spectra of the Au valence band at the Fermi energy (ϵ_F). Additionally, spectra close to the (ϵ_F) were taken with a resolution of 150 meV. The angle between the electron spectrometer and photon propagation is fixed at 90 °. The photons are p-polarized; that is, the electric field vector is in the plane of incidence and always pointing in the direction of the electron spectrometer. A near-normal emission ($\theta \approx 2°, \ldots, 5°$) angle was used for electron detection. (Note that the angle is not well defined for fractured bulk samples because of surface roughness.) The measurements were taken at sample temperatures of 20 and 300 K.

III. RESULTS AND DISCUSSION

A. Structure determination by EXAFS and aXRD

Synchrotron-based absorption and scattering experiments (EXAFS and aXRD) were performed because of the problems in unambiguously determining the structure in laboratory XRD experiments using Mo K_α radiation. In the first step, the raw EXAFS spectra allow us to select the energies of the K absorption edges of the contributing elements that are used for the aXRD. The aXRD data then allow for a better description of the long-range order and crystalline structure to be used for the fitting of the EXAFS data. Figure 2 displays the x-ray absorption spectra (XAS) taken at the K edges of Co, Mn, and Ge. The XAS spectra correspond to f'' and exhibit the typical EXAFS intensity modulations. The program FPRIME[12] was used to find the f' parameter from an Kramers-Kronig analysis. (f' and f'' are the real and imaginary parts, respectively, of the atomic scattering factor.)

Figure 3 compares the results of the aXRD experiments performed at a sample temperature of 300 K. At off-resonant excitation (7112.27 keV) the fcc 111 and 200 superstructure reflections of the ordered $L2_1$ structure are weakly visible. The situation is different if the energy is moved closer to the K absorption edge of Mn at 7112.27 keV, where a strong enhancement of the 111 reflection is observed. The 200 reflection appears already for samples with $B2$ structure, whereas 111 appears alone in the $B32$ structure.

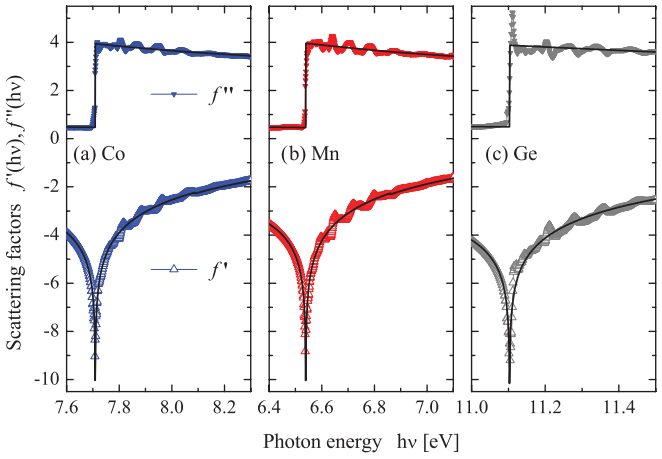

FIG. 2. (Color online) K-edge absorption spectra and Kramers-Kronig analysis of the Co_2MnGe EXAFS data. The absorption spectra correspond to f''. For all spectra, the intensity was normalized to the photon intensity and afterward to an *edge jump* of one after subtracting a constant background.

The appearance of both together is indicative for $L2_1$ or DO_3 type structures. The higher intensity of the 111 reflection compared to 200 gives clear evidence for the $L2_1$ structure as the dominant phase in the sample.

The aXRD data were analyzed in more detail using Powdercell[13] with anomalous scattering parameters calculated by SCATFAC.[14] The results of the Rietveld refinement are summarized in Table I. The results from the measurement with Mo K_α radiation are given for comparison. The lattice parameter averaged over the high-resolution synchrotron measurements taken with different energies is $\bar{a} = (5.7477 \pm 0.0017)$ Å.

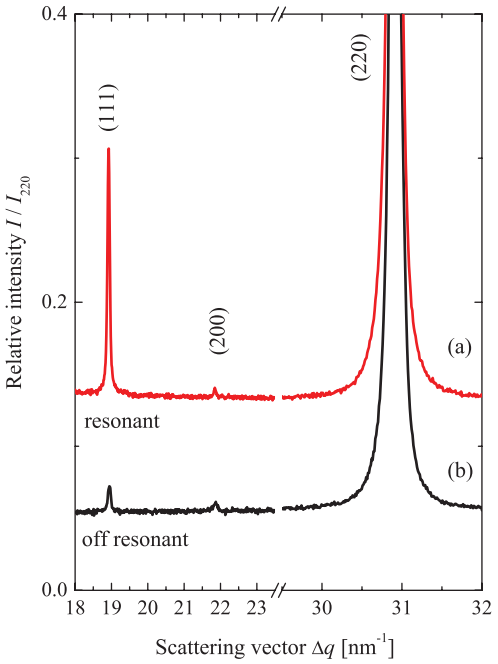

FIG. 3. (Color online) Anomalous XRD of polycrystalline Co_2MnGe. The data were taken at room temperature using synchrotron radiation for excitation. The excitation energy was set to (a) 6539.89 eV (Mn resonant) or (b) 7112.27 eV (off-resonant).

TABLE I. Anomalous XRD of polycrystalline Co_2MnGe. The data were taken resonant at the Mn K absorption edge (6539.89 keV), off-resonant (7112.27 eV), and with Mo K_α radiation (17479.2 eV). The R values of the refinement are given in percent.

	Mn resonant		Off-resonant		Mo K_α	
	exp.	calc.	exp.	calc.	exp.	calc.
I_{111}/I_{220}	0.207	0.207	0.019	0.023	0.025	0.019
I_{200}/I_{220}	0.041	0.048	0.007	0.006	0	0.002
R_p	5.88		3.37		6.24	
R_{wp}	8.61		9.49		9.84	

The analysis of the aXRD data makes the $L2_1$ structure of Co_2MnGe clearly evident.

Figure 4 summarizes the results of the EXAFS analysis of the x-ray absorption spectra taken at the K edges of Co, Mn, and Ge. The XAS spectra were analyzed in accordance with the standard procedure of data reduction,[15] using IFEFFIT.[16] FEFF was used to obtain the phase shift and amplitudes.[17] The EXAFS signal $\chi(k)$ was extracted and then Fourier transformed using a Kaiser-Bessel window with a Δk range of 9.0 Å^{-1}. The $\chi(k)$ curves display the characteristic pattern of a cubic structure, as expected for this Heusler compound. The Fourier transforms (FTs) display two well-defined peaks at about 2.2 and 4.5 Å (uncorrected for the phase shift), which correspond to the scattering contribution in the coordination shell and next nearest neighbors. Multiple scattering contributions appear in the region between the two main peaks. The best-fitting curves (gray lines) of the EXAFS signal and FT modulus considering the $L2_1$ structure are also displayed in Fig. 4. Single and multiple scattering events were considered in the fitting procedure. The overall fitting procedures of all elements contained in Co_2MnGe lead to physically reasonable numbers close to those of the theoretical structural model. A quantitative analysis extracted from the EXAFS data is presented in Table II. The obtained amplitude-reduction term (S_0^2) varied between 0.70 and 0.84. The shifts in distances

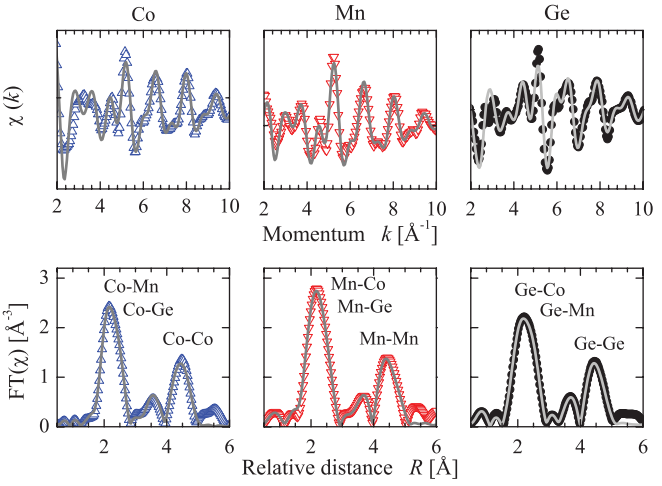

FIG. 4. (Color online) EXAFS oscillations extracted from the x-ray absorption measurements at the K edges of Co, Mn, and Ge, along with the corresponding Fourier transforms (symbols) and best-fitting results (gray lines).

TABLE II. Co_2MnGe EXAFS data analysis. Results are obtained from the quantitative analysis of the EXAFS data for the Co, Mn, and Ge K edges, considering the coordination numbers (N) of the $L2_1$ structure. The best fitting provided the next-neighbor distances (d), Debye-Waller factor σ^2, and R factor for each absorbing atom.

Pair	N	d (Å)	σ^2 (10^{-2} Å^2)	R (%)
	Co K edge (7709 eV)			
Co-Mn	4	2.47 ± 0.02	0.63 ± 0.02	
Co-Ge	4	2.47 ± 0.02	0.63 ± 0.02	0.89
Co-Co	6	2.85 ± 0.02	0.81 ± 0.05	
Co-Co	12	4.04 ± 0.03	1.2 ± 0.1	
	Mn K edge (6539 eV)			
Mn-Co	8	2.47 ± 0.02	0.63 ± 0.02	
Mn-Ge	6	2.86 ± 0.02	0.70 ± 0.1	0.49
Mn-Mn	12	4.08 ± 0.04	1.0 ± 0.1	
	Ge K edge (11103 eV)			
Ge-Co	8	2.47 ± 0.02	0.63 ± 0.02	
Ge-Mn	6	2.86 ± 0.02	0.70 ± 0.1	0.57
Ge-Ge	12	4.04 ± 0.04	0.80 ± 0.1	

(ΔR) were also small, with a typical variation from -0.02 to -0.07 Å. Excellent agreement between the data and the theoretical $L2_1$ model was accomplished, as demonstrated in Fig. 4 and by the low R factors (<1% in Table II).

B. Electronic structure calculations

The electronic and magnetic structures were investigated with *ab initio* calculations using WIEN2K.[18] The details of the calculations are described in Ref. 19. As a starting point the lattice parameter was optimized by using the generalized gradient approximation in the parametrization of Perdew-Burke-Enzerhof.[20] The relaxed lattice parameter is $a = 5.7301$ Å at a bulk modulus of 317 GPa. Figure 5 shows the band structure of Co_2MnGe calculated for the relaxed lattice parameter. The compound is a half-metallic ferromagnet with a gap in the minority states. This finding is in good agreement with previously reported calculations.[21] The size of the minority gap amounts to $\Delta E = 0.58$ eV. The top of the minority valence band is about 70 meV below ϵ_F. Owing to the half-metallic character the magnetic moment in the primitive cell is $5\mu_B$, in excellent agreement with the Slater-Pauling rule.[22]

Additional details of the electronic structure are revealed in Fig. 6, which shows not only the total but also the site, orbital momentum, and symmetry-resolved DOS. The states below -9 eV are of a_{1g} character and mainly located in the vicinity of the Ge sites. The occupied d states are found between ϵ_F and -5 eV. The existence of the minority band gap at ϵ_F is obvious from all DOS plots. Its size and position are exclusively determined by Co states [compare Figs. 6(a) and 6(b)]. At the minority valence-band maximum the Co states are of t_{2g} character whereas they have e_g character at the minimum of the minority conduction band [see Fig. 6(d)]. The electrical conductivity of the compound is determined by the strongly dispersing majority bands at ϵ_F. They are rather delocalized and cannot be assigned to a particular site of either Co or Mn. From Fig. 6(d),

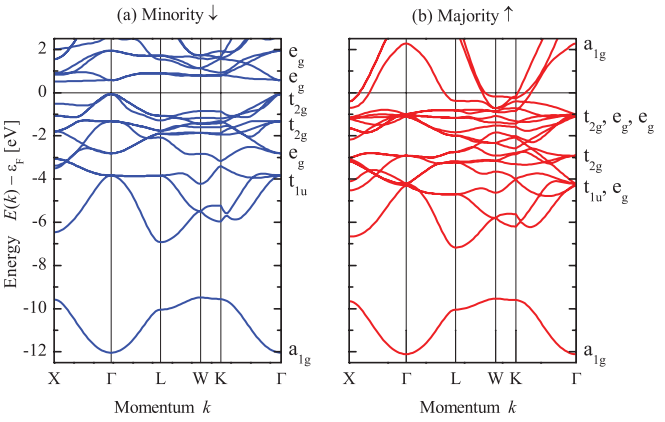

FIG. 5. (Color online) Calculated band structure of Co_2MnGe for (a) minority states and (b) majority states, respectively. The irreducible representations of the states at the Γ point are marked for O_h symmetry. Note that the subscripts g and u are given in the standard notation for states with even and odd parity with respect to the orbital angular momentum. The series of irreducible representations for majority states being close together is given from left to right, starting with the topmost state [see also the scheme in Fig. 7(c)].

we see that the d electron densities located close to Co exhibit a nearly uniform distribution over the energy range of the valence bands, independent of the symmetry or spin character. In contrast, the valence electrons attributed to the Mn site exhibit a pronounced localization at -1 eV (e_g) and around -3 eV (t_{2g}) in the majority channel. This leads to a distinct exchange splitting of 2.8 eV between the occupied majority and unoccupied Mn e_g states. The spin-averaged decomposition of the number of occupied d states localized in the vicinity of Co or Mn is summarized in Table III.

Given the previous considerations it should be noted that many of the electrons are located in the interstitial space between the muffin-tin spheres describing the atoms of the primitive cell and thus cannot be specifically attributed either to one or another of the contributing elements or a specific orbital momentum. At this point—and before continuing with

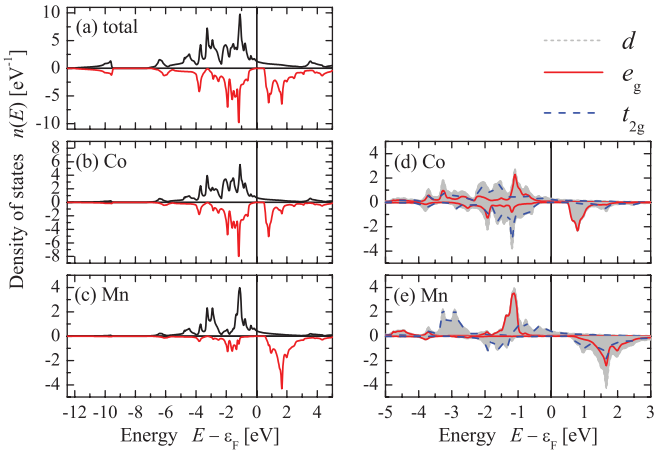

FIG. 6. (Color online) Partial density of states of Co_2MnGe. [Note the different scales of the $n(E)$ plots.]

TABLE III. Site-resolved magnetic moments (m) and d state occupancy n_d of Co and Mn in Co_2MnGe. All magnetic moments (m) are given in μ_B.

	Co			Mn		
	d	e_g	t_{2g}	d	e_g	t_{2g}
n_d	7.4	2.7	4.7	5.1	1.9	3.1
m	1.0	0.9	0.1	3.0	1.55	1.45

the magnetic moments—recall that, from the objective point of view of the solid, all electrons are indistinguishable whereas only a subjective observer divides the solid arbitrarily into spheres or other objects of a given but virtual size. Strictly speaking, the dispersion $E(k)$, total density of states, and total magnetic moments are the only well-defined ground-state quantities but they are not the site-resolved ones.

Galanakis and co-workers[21] explained the half-metallicity of Co_2MnGe by a particular molecular orbital coupling scheme. To develop the model, they had to assume, however, that the Co atoms are in an environment with O_h symmetry. This assumption is incorrect even though the total symmetry of the cubic cell of $L2_1$ Heusler compounds is O_h. The sites occupied by Co have no inversion symmetry and carry T_d symmetry, as is evident from the primitive cell shown in Fig. 7(b). In contrast, the sites occupied by Mn and Ge exhibit O_h symmetry. Alternative molecular orbital diagrams are developed in Ref. 2 for the examples of half-metallic Co_2MnSi and semiconducting Fe_2VAl. Figure 7(c) shows schematically, without assumption of any particular molecular orbital coupling scheme, directly the order of the states at the Γ point of Co_2MnGe. The half-metallic character determined by the band filling of the minority states is obvious. The successive complete filling of the minority bands (a_{1g}, t_{1u}, e_g, $2 \times t_{2g}$) by 12 electrons leads to a quasi-closed-shell character. The energy scheme for the majority electrons is considerably different from that of molecular orbital models. It is seen that the additionally occupied doubly degenerate states are pushed at Γ below the triply degenerate states. Finally, the strongly dispersing high-lying (a_{1g} and t_{1u} character at Γ) majority bands start to cross ϵ_F and bring the majority electronic structure close to a simple metal [compare Figs. 5 and 7(b)]. Both effects together show the limits for the application of molecular orbital schemes. The latter has another important consequence: When the two additional e_g states are occupied one reaches compounds with 28 valence electrons overall, which exhibit a total spin moment of $4\mu_B$. At that valence electron concentration the "localized" weakly dispersing bands are used up and a further increase will need to fill "delocalized" states with strong band dispersion. The filling of these bands needs a rather large exchange interaction to split the occupied and unoccupied localized states. It seems that there is a limit at which the exchange interaction cannot be increased further. This limit is reached when the compound has 30 valence electrons, that is, when about two "delocalized" majority bands are filled. This explains why Heusler compounds with magnetic moments of considerably more than $6\mu_B$ are not known, in contrast to fully localized, nondispersing molecular orbital schemes that suggest $7\mu_B$ as a limit.[21]

The calculated ground-state magnetic moment of $5\mu_B$ in the primitive cell agrees well with the measured saturation magnetic moment of $4.982\mu_B$ at 5 K. The calculations reveal that the site-resolved moments per atom are about 1 and 3 μ_B at Co and Mn, respectively. Besides the site-specific moments, the symmetry-resolved moments are of interest, that is, the distribution of the moments arising from the e_g and t_{2g} states. The site- and symmetry- resolved values are summarized

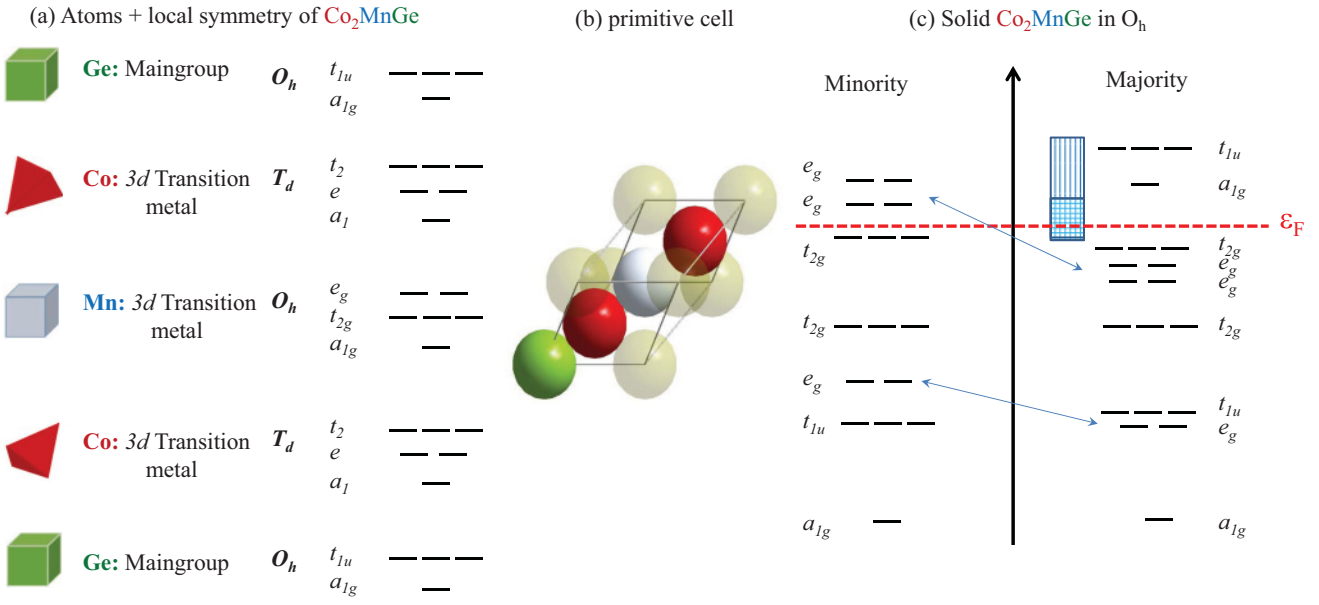

FIG. 7. (Color online) Schematic illustration of the orbitals and states in Co_2MnGe. The local symmetries and basic states of the atoms in an environment with O_h symmetry are shown in (a). The primitive fcc cell with a base of four atoms as shown in (b) reveals the center of inversion of the O_h symmetry group. (c) is a schematic of the states at the Γ point of the solid with O_h symmetry. The box in (c) indicates that the unoccupied majority states with a_{1g} and t_{1u} character are delocalized and smeared over a wide band of energies in k space.

in Table III. It is seen that the site-resolved moments arise exclusively from the d electrons for both constituents Co and Mn. At the Co site one obtains $n_d^{\mathrm{Co}} = 7.4$ d states, from which 4.7 d states have t_{2g} character; however, the main part of the moment arises from e_g states, which have a lower occupancy of $n(e_g) = 2.7$. The situation is different at the Mn site, where one has a d state occupancy of $n_d^{\mathrm{Mn}} = 5$ with a $n(e_g)/n(t_{2g})$ ratio of about 2/3. At Mn, the d states of both symmetries contribute uniformly about $1.5\mu_B$ to the site-resolved moment.

The site-resolved magnetic moments are in good agreement with measurements using x-ray magnetic dichroism (XMCD), which resulted in spin magnetic moments of $m_{\mathrm{Co}} = 0.93\mu_B$ and $m_{\mathrm{Mn}} = 3.25\mu_B$.[23–26]

C. Hard x-ray photoemission

1. *Core-level spectroscopy*

Hard x-ray core-level spectra of Co_2MnGe were measured to investigate the spin-orbit splitting as well as the exchange interaction of the unpaired valence electrons with the core holes. The spectra of the Co $2p$ and Mn $2p$ core levels are shown in Figs. 8(a) and 8(b), respectively. The spectra are taken at low temperature (16 K) with an excitation energy of about 8 keV.

Figure 9 shows the hard x-ray photoelectron spectrum of Co_2MnGe in the energy range of the semicore level. (Note the low intensity of the valence band.) Details of the energies are summarized in Table IV. Obviously, the spin-orbit splitting of the Ge $3p$ state is more pronounced than the one of the Co $3p$ state even though the nuclear charge Z_{Ge} is only five higher than Z_{Co}.

Besides the spin-orbit splitting of the p states, the spectra shown in Figs. 8 and 9 exhibit several satellites that result from other effects. Typical is the appearance of metallic satellites or multiplet splittings from the exchange interaction. The metallic satellites arise from plasmon losses or excitation of interband transitions. The spin-orbit splitting (Δ_{SO}), exchange splitting (Δ_{EX}), and metallic satellites (Δ_{MS}) were determined

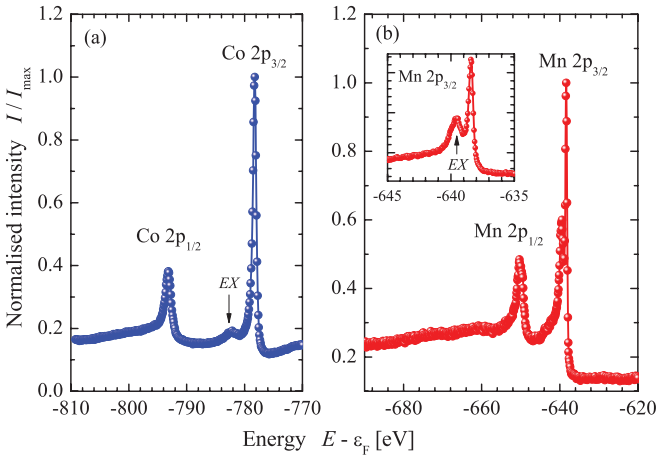

FIG. 8. (Color online) High-energy photoelectron spectra of the (a) Co $2p$ and (b) Mn $2p$ core level of Co_2MnGe. The spectra are excited by a photon energy of $h\nu = 7.9392$ keV at low temperature (16 K). The inset in (b) shows the details of the Mn $2p_{3/2}$ state on a stretched scale.

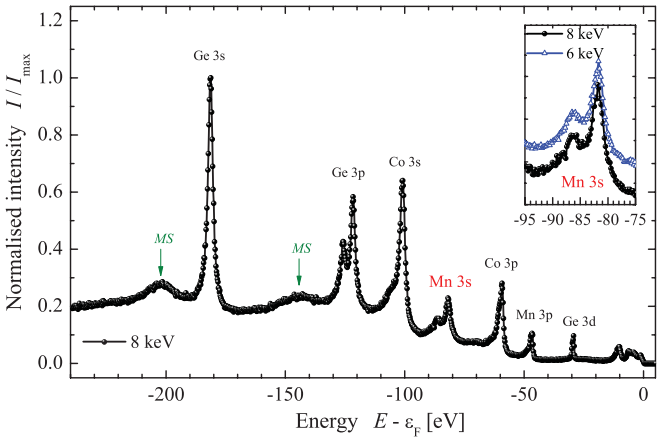

FIG. 9. (Color online) Semi-core-level spectra of Co_2MnGe. The spectrum was taken at 300 K and excited by a photon energy of $h\nu = 7.9392$ keV. The inset shows a magnified view of the Mn $3s$ state taken at different photon energies (5.9468 or 7.9392 keV).

for selected core and semi-core level and the results are summarized in Table IV.

Most interesting is that the Mn $3s$ state exhibits a well-distinguished exchange splitting of $\Delta_{\mathrm{ex}} = 4.68$ eV [see inset in Fig. 9(b)]. The intensity ratio between the main $3s$ line and the exchange-split satellite appears to be independent of the excitation energy. Such a splitting was not observed in previous work on Co_2MnSi.[27] In analogy to the Co $2p$ spectra, the Mn $2p$ core level shows $\Delta_{\mathrm{SO}} = 12.1$ eV. Different from the Co $2p$ spectra, the multiplet splitting of the Mn $2p_{3/2}$ state is clearly revealed. The inset of Fig. 8(b) demonstrates the occurrence of the multiplet splitting at the Mn $2p_{3/2}$ state by $\Delta_E = 1.17$ eV. It was shown theoretically and experimentally for the case of Mn that the Coulomb interaction of the $2p$ core hole and the $3d$ valence electrons leads to the splitting of the Mn $2p_{3/2}$ level into several main sublevels[28] caused by the existence of more than one possible excited ionic state during ejection of electrons from the p core level. The splitting is less pronounced at the $2p_{1/2}$ state owing to the broadening of the line caused by a shorter lifetime of the hole in the $2p_{1/2}$ region compared to the $2p_{3/2}$ one.

In atoms, the multiplet splitting is due to the interaction of the nl^{-1} core hole with the polarized open valence shell. It is expected that the core hole (here $3s^1$ or $2p^5$) in solids interacts with the polarized d states of the valence band. Assuming that the atomic character of the valence electrons is—at least partially—retained in the solid one is able to use the well-

TABLE IV. Core-level splittings in the Co_2MnGe spectra. Given are spin-orbit splitting Δ_{SO}, exchange splitting Δ_{EX}, and metallic satellites Δ_{MS} of selected core states of Co_2MnGe. All energies are given in eV.

	Co $2p$	Mn $2p$	Ge $3p$
Δ_{SO}	14.91	11.72	4.13
Δ_{EX1}	3.95	1.17	22.78
Δ_{EX2}	2.18	2.76	18.65
Δ_{MS}	7.70	0.95	—

known multiplet theory to explain the observed splittings in the spectrum.[29–33]

Now, concentrating on the Mn atoms in Co_2MnGe, one sees that the description becomes complicated as it is not *a priori* clear what ionic state the Mn adopts in the metal. From the calculations (see Table III) one has Mn d^5, neglecting all other shells. However, some of the d electrons are delocalized in the metal and may not contribute to the coupling.

Assume a Mn^{2+} or Mn^{3+} ionic state with a $^6S_{5/2}$ or $^5D_4$ ground state in **LSJ** coupling. Note that the description of the ground states of neutral $Mn^0(4s^23d^5)$ and $Mn^{2+}(4s^03d^5)$ are principally the same because the filled $4s^2$ shell does not contribute. According to the dipole selection rules the following transitions take place for the various ground and excited states for excitation of ns core levels (here for the example of $3s$):

(i) from $3s^23d^5$ ($^6S_{5/2}$)
to $\{[3s^13d^5\ (^{5,7}S_J)] + \epsilon(p)\}(^6P_{7/2,5/2,3/2})$,

(ii) from $3s^23d^4$ ($^5D_4$)
to $\{[3s^13d^4\ (^{4,6}D_J)] + \epsilon(p)\}(^5P_{J'}, ^5F_{J'})$,

or for np core levels (here for the example of $2p$):

(iii) from $2p^63d^5$ ($^6S_{5/2}$)
to $\{[2p^53d^5\ (^{5,7}P_J)] + \epsilon(s,d)\}(^6P_{7/2,5/2,3/2})$,

(iv) from $2p^63d^4$ ($^5D_4$)
to $\{[2p^53d^4\ (^{4,6}F_J, ^{4,6}P_J)] + \epsilon(s,d)\}(^5P_{J'}, ^5F_{J'})$.

$\epsilon(p)$ or $\epsilon(s,d)$ denote the ejected electrons with kinetic energy ϵ_k and orbital angular momentum $l' = 1$ or $l' = 0,2$ for ionization of the $3s$ or $2p$ shells, respectively. The final total angular momentum related to the $^5D_4$ ground state can take the values $J' = 3$, 4, or 5. It is obvious that the intermediate ionic states always have spin values of $\mathbf{S}(d^5) = 5,7$ or $\mathbf{S}(d^4) = 4,6$. From this point of view, the splitting observed in emission from $3s$ or the two groups of transitions at the $2p$ may be assigned by the spin-exchange splitting of the ionic states. The remaining smaller splittings observed in emission from the $2p$ shell correspond to states with different total angular momentum J of the $^7P_{J=4,3,2}$ and $^5P_{J=3,2,1}$ intermediate ionic states for Mn^{2+} (or similar for the $^5D_4$ ground state of Mn^{3+}). For the $^6S_{5/2}$ ground state, in particular, $^7P_4$ corresponds to the ionic state with highest energy in the spectrum (the lowest final-state energy).

The observed intensity ratio of the two transitions at the Mn $3s$ state is 2.5, which is considerably larger than the expected 6:4 = 1.5 ratio for a Mn^{3+} d^4 ($^5D_4$) ground state [7:5 = 1.4 for d^5 ($^6S_{5/2}$)] when calculating it from the spin multiplicity ($2\mathbf{S} + 1$) of the intermediate ionic states. Therefore, atomic type multiplet calculations were performed using de Groot's program CTM4XAS[34] to provide more detail of the ionic state of Mn in Co_2MnGe. The details of the multiplet description and applied methods are found in Refs. 29 and 32. For the $3s$ excitation, the Slater integrals were scaled to 90% of their value from the Hartree-Fock calculations. The same reduction was used for the $2p$ excitation where the LS coupling parameter for the ground state was also scaled to 90%. A Lorentzian of 100 meV width for the lifetime broadening and a line broadening by Gaussians of 240 meV were used with respect to the experimental resolution.

To understand the electronic state of Mn in Co_2MnGe, the photoemission spectra of the $2p$ and $3s$ states for the Mn^{2+} as well Mn^{3+} were calculated and compared to the

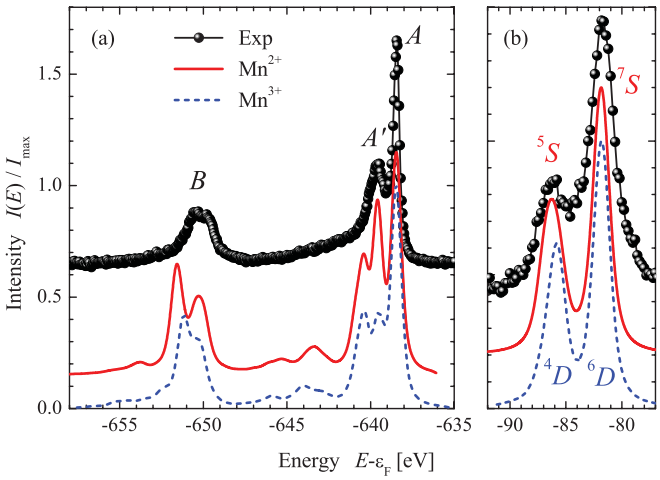

FIG. 10. (Color online) Comparison of the experimental and calculated core-level spectra of Mn in Co_2MnGe. The Mn$2p$ spectra are shown in (a) and $3s$ spectra in (b). The calculations were performed for d^5 and d^4 configurations of Mn, resulting in $^6S_{5/2}$ (full lines) and $^5D_4$ (dashed lines) ground states, respectively. In (a) the states A and B correspond in the single-particle picture to the spin-orbit-split $2p_{3/2}$ and $2p_{1/2}$ initial states. In the many-electron description the notation will depend on the assumed ground state (see text for details).

investigated high-energy photoelectron spectra. The results are shown in Fig. 10. For Mn $3s$ the splitting of both the Mn^{2+} and Mn^{3+} ionic states fit the experimental data very well. Different lines of the underlying multiplet structure are not resolved. The calculated ^4D-^6D splitting of Mn^{3+} is slightly too small compared to the experimental value or to the ^5S-^7S splitting when assuming Mn^{2+}. In both cases the branching ratio does not fit the experiment. The situation is different for the $2p$ excitation where the splitting is not only determined by the Coulomb interaction but also by the spin-orbit interaction. By using the same scaling for the Slater integrals as for the $3s$ excitation, the main splitting between the multiplet components A and B at about -640 and -650 eV fits the experiment better when assuming a Mn^{3+} configuration. The details of the A-A' splitting of the spectrum at about -640 eV make clear that neither Mn^{2+} nor Mn^{3+} ionic states explain the spectra correctly. Comparing the intensities shows that the experimental spectrum is obviously between these cases. This means that one has either a mixture of d^4 and d^5 or, what is more realistic for a metallic solid, a formal $d^{4.x}$ configuration with respect to the incomplete localization of the d electrons at the Mn site. This might be seen as contradicting the electronic structure calculations in which 5.1 d electrons are found at Mn (see Table III). Above, the "size of Mn" was haphazardly set to touching spheres; if a sphere with a 15% smaller radius is chosen then one finds only 4.6 d electrons, without changing any other property of the electronic structure. One should be aware that, by taking this as the size of Mn in the solid, it becomes impossible to figure out the exact numbers of *localized* and *delocalized* electrons.

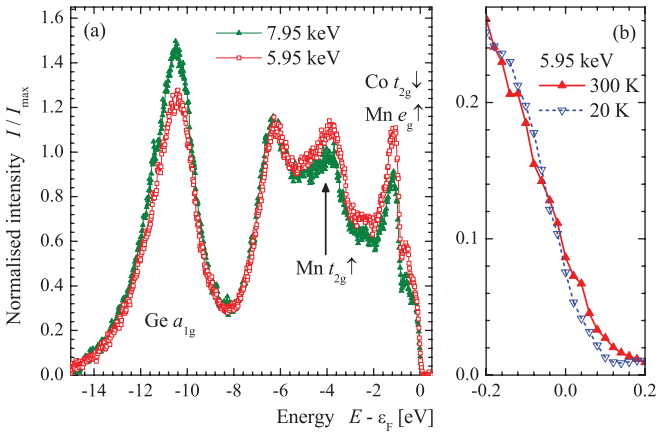

FIG. 11. (Color online) Valence-band spectra of Co_2MnGe (a) taken at 20 K excited by different photon energies (5.9468 or 7.9392 keV) and (b) in the vicinity of the Fermi energy at different temperatures ($h\nu = 5.9468$ keV).

2. *Valence-band spectroscopy*

In the next step, the valence states of Co_2MnGe were investigated by photoelectron spectroscopy. Figure 11(b) compares the valence-band spectra of Co_2MnGe taken at low (20 K) and high (300 K) temperature at an excitation energy of about 6 keV. The changes in the spectra at different temperatures are unremarkable. The only effect is the expected broadening of the spectra and the slight smearing of the states at the Fermi edge caused by the change of the Fermi-Dirac distribution while going from 20 to 300 K. This observation is in accordance to the work on Co_2MnSi[27,35] where also no temperature-dependent changes were detected.

Figure 11(a) compares the valence-band spectra taken with different photon energies of about 6 and 8 keV. The differences in the spectra are caused by the different weights of the partial photoionization cross sections for s, p, and d electrons at different excitation energies. With increasing energy the cross sections for d electron excitation decrease faster than those for s or p electrons (see Refs. 36 and 37). Therefore, the contribution from d electrons is more pronounced at lower energy.

The maximum of the emission from the a_{1g} states appears at -10.5 eV, which is about 1 eV lower compared to the calculated DOS. The maximum at about -3.9 eV corresponds to an excitation of the Mn t_{2g} minority states; its center is about 0.9 eV lower compared to the center of the states in the calculated DOS. The calculated site-resolved DOS exhibits pronounced Co and Mn e_g majority states as well as Co t_{2g} minority states at about -1 eV, where a strong maximum is observed in the spectrum. A pronounced influence of a correlation energy can thus be excluded, as proven by the small energy shifts between the experimental spectrum and calculated DOS. The observed energy shifts increase when moving further away from ϵ_F. This points clearly to lifetime effects: The holes at ϵ_F have a longer lifetime compared to those at lower energies. Accounting for the lifetime effects by increasing the imaginary part in the self-energy of the photoexcited electrons results in observed states that not only have an increased width when moving away from ϵ_F but also exhibit an increase of the energy shift. States that are farther away from ϵ_F are more strongly influenced because of the nonlinearity of the self-energy, being zero at ϵ_F and rising within a small energy range (a few eV) to its final value. It is concluded that the observed shifts are due to the photoemission process and are not related to an electron-electron interaction in the ground state.

D. Mechanical properties

In most cases only the electronic structure and magnetic properties of Heusler compounds are reported and used to compare theory and experiment. There are, however, other physical quantities available from the calculations and experiments that are important for later applications of the materials. Therefore, the mechanical, vibrational, and transport properties are reported in the following.

The mechanical properties were calculated in addition to the optimization of the lattice parameters. Besides the bulk modulus B, which is found directly from the equation-of-states fit,[38,39] the elastic constants c_{ij} were calculated for Co_2MnGe as well as the isovalent compound Co_2MnSi. The elastic stability criteria for the cubic structure are found from the elastic constants (c_{ij}).[40–42] The necessary conditions are

(a) $c_{11} + 2c_{12} > 0$,
(b) $c_{44} > 0$,
(c) $c_{11} - c_{12} > 0$;

that is, the bulk, c_{44} shear, and tetragonal shear moduli are all positive. The elastic anisotropy is defined for cubic crystals by

$$A_e = \frac{2c_{44}}{c_{11} - c_{12}}. \quad (1)$$

A_e also allows a decision about the structural stability. Materials exhibiting large A_e ratios show a tendency to deviate from the cubic structure. Table V compares the mechanical properties of Co_2MnSi and Co_2MnGe. The elastic constants were calculated by applying isotropic strain as well as volume-conserving tetragonal and rhombohedral strains to the optimized cubic primitive cell. The bulk modulus of the Si-containing compound is about 16% larger than that of the Ge-based compound. The elastic constants of both compounds follow the general inequality $B > c_{44} > G > 0$, where G is

TABLE V. Mechanical properties of Co_2MnZ (Z = Si, Ge). Calculated bulk (B), Young's (E), and rigidity (G) moduli as well as the elastic constants c_{ij} are given in GPa; Poison's ratio (ν) and elastic anisotropy (A_e) are dimensionless quantities. Vickers hardness HV1 was measured with a load of 9.806 N and is given in kg/mm^2.

	Co_2MnSi	Co_2MnGe
c_{11}	290	250
c_{12}	179	180
c_{44}	158	132
B	216	203
G	104	77
E	269	206
ν	0.29	0.33
A_e	2.83	3.76
HV1	807 ± 14	741 ± 2

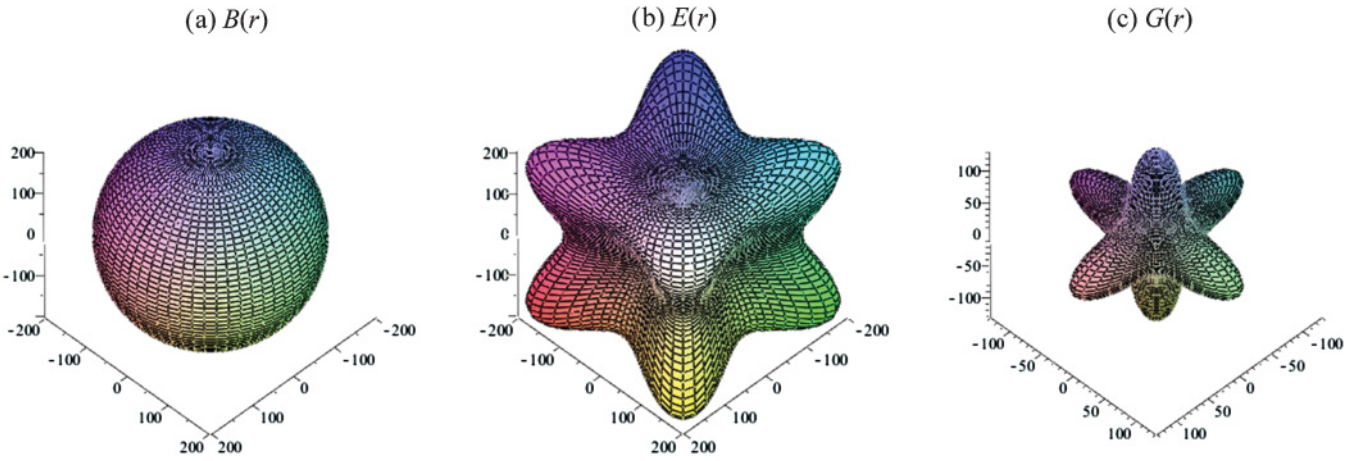

FIG. 12. (Color online) Calculated spatial distribution of the bulk (B). Young's (E), and rigidity (G) moduli of Co_2MnGe.

Voigt's shear or rigidity modulus. Both A_e and the elastic stability criteria show that the compounds are stable in the cubic $L2_1$-type crystal structure.

Figure 12 displays the three-dimensional distribution of the bulk (B), Young's (E), and rigidity (G) moduli of Co_2MnGe. (Those of Co_2MnSi are not shown, but they have a similar shape because of the close values of the elastic constants.) The bulk modulus is isotropic as mentioned above. By comparing the distribution of the remaining two moduli it is obvious that Young's modulus is largest in the ⟨111⟩-type directions whereas the rigidity modulus is largest in the $<100>$-type directions, that is, along the cubic axes.

From the elastic constants, or say better the elastic moduli, one is able to calculate the speed of sound and Debye temperature Θ_D^{acc} in the approach given by Anderson.[43] For Co_2MnGe one finds in the acoustical approximation $\Theta_D^{\text{acc}} = 554$ K from the values in Table V.

The hardness (HV) was measured using a low-load Vickers hardness tester (Zwick, type Z3212). The load used to evaluate the Vickers microhardness (HV1) was $F = 9.806$ N ($P = 1$ kg). The Vickers hardness is determined from

$$\text{HV} = \frac{1.8544P}{d^2}, \tag{2}$$

where d is the diagonal length of the impression of the diamond probe (pyramid with apex angle $= 135°$). The Vickers hardness is not directly proportional to the elastic bulk modulus but indirectly depends on the elastic constants. The trend, however, is obvious: The Si-containing compound with higher bulk modulus also has a 8% higher hardness compared to the Ge-based compound.

The Chin-Gilman parameter $c_{\text{CG}} = H/c_{44}$ is the ratio of the hardness number H to the shear modulus.[44,45] For cubic crystals the latter is the elastic constant, c_{44}. Chin showed that it varies systematically with the type of chemical bonding in the crystals.[46] For cubic crystals the average values of metallic, ionic, or covalent systems are $c_{\text{CG}}^{\text{met}} = 0.006$, $c_{\text{CG}}^{\text{ion}} = 0.01$, or $c_{\text{CG}}^{\text{cov}} = 0.1$, respectively.[46,47] The obtained values c_{CG} taken from measured hardness and calculated elastic constants for Co_2MnSi and Co_2MnGe are 0.05 and 0.06, respectively. These values prove that the type of bonding of the compounds is close to covalent.

E. Vibrational properties

The vibrational properties of Co_2MnGe were calculated by means of PHONON[48] on the basis of the results from WIEN2K. The primitive cell containing four atoms was enlarged to a cell with 16 distinguished atoms to calculate the Hellmann-Feynman forces for the phonon analysis. For these calculations, a force convergence criterion of 10^{-4} Ry a_{0B}^{-1} was used in addition to the energy convergence criterion. The results of the phonon calculations are based on the spin-polarized electronic structure calculations. Figure 13 shows the calculated phonon dispersion $h\nu(q)$ and the accompanied density of states $\rho(\omega)$ of Co_2MnGe.

Figure 14 compares the temperature dependence of the calculated phonon $C_L(T)$ as well as the electron $C_e(T)$ part of the specific heat to the measured specific heat $C(T)$. Above 240 K the sum of $C_L(T)$ and $C_e(T)$ agrees well with the measured specific heat $C(T)$. The small differences between measured and calculated values at low temperature ($T < 100$ K) reveal that the specific heat is dominated by the phonon contribution. Deviations at higher temperature are caused by the fact that the measured C contains not only the

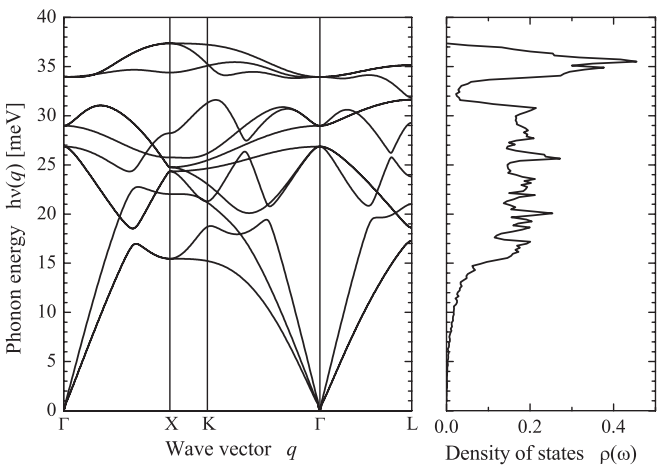

FIG. 13. Phonons of Co_2MnGe. (a) Phonon dispersion and (b) corresponding density of states.

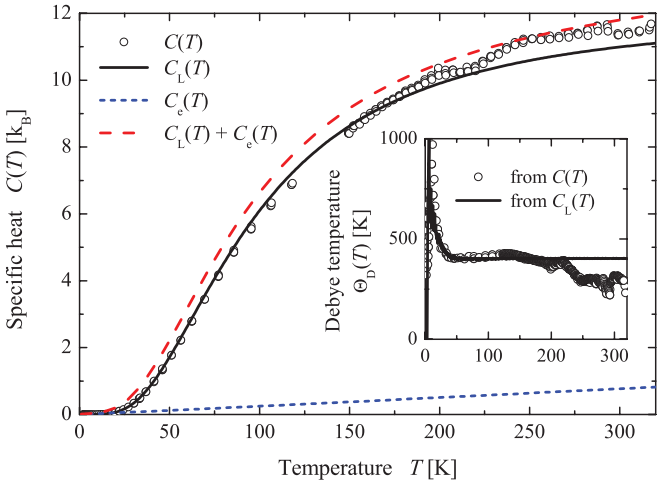

FIG. 14. (Color online) Specific heat of Co_2MnGe. $C(T)$ is the measured specific heat containing also electron and magnon contributions; $C_L(T)$ and $C_e(T)$ are the calculated lattice and electron specific heat, respectively. The inset shows the Debye temperature calculated from a fit to the $C(T)$ data.

lattice contribution but also contributions from electrons and magnons.

The temperature-dependent heat capacity is expressed according to a suggestion from Ref. 49 as a polynomial sum [Eq. (3)]. A fit of the data in the low-temperature range to

$$C(T) = A \cdot T^{-2} + \gamma \cdot T + \beta \cdot T^3 \qquad (3)$$

results in values of $A = (35.15 \pm 0.06)$ mJ K/mol, $\gamma = (23.2 \pm 1.4)$ mJ/(mol K^2), and $\beta = (1.46 \pm 0.03)$ μJ/(mol K^4). The Debye temperature Θ_D is found by fitting the measured or calculated specific heat to the Debye model. The result is shown in the inset of Fig. 14. The Debye temperature calculated from $C_L(T)$ is $\Theta_D = 403$ K in the high-temperature limit ($T > 50$ K). The temperature dependence of Θ_D calculated from the measured specific heat $C(T)$ does not clearly approach the high-temperature limit, which is mainly due to experimental uncertainties as well as the increasing influence of the electron and magnon specific heats at higher temperatures. The Debye temperature derived from the specific heat is lower compared to the acoustic value derived from the elastic constants ($\Theta_D < \Theta_D^{acc}$; see above), pointing to the influence of the high-lying optical modes.

The calculated thermal displacements $\langle u^2 \rangle$ at 300 K are 4.2×10^{-3}, 4.1×10^{-3}, and 3.9×10^{-3} Å^2 for Co, Mn, and Ge, respectively. The average value of 4.06×10^{-3} Å^2 is about half of the average Debye-Waller factor $\sigma^2/2 = 3.9 \times 10^{-3}$ Å^2 found in the EXAFS measurements (see Table II). The values of the mean square displacement and the Debye-Waller factor depend on the underlying model and the factor of about 2 between $\langle u^2 \rangle$ and σ^2 is explained in detail in Ref. 50.

F. Transport properties

The measured transport properties of Co_2MnGe are summarized in Fig. 15. The electric resistivity $\rho(T)$ data from 5 to 300 K were obtained by a standard linear four-point contact method. The results shown in Fig. 15(a) exhibit a

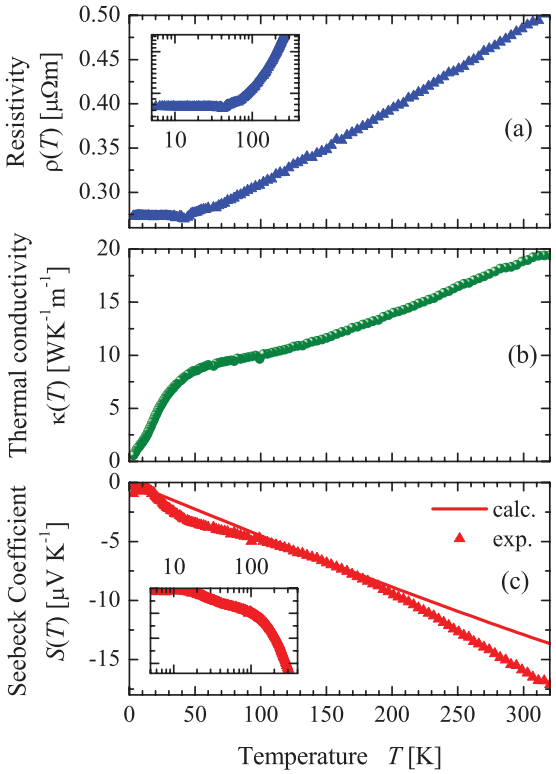

FIG. 15. (Color online) Temperature dependence of the transport properties of Co_2MnGe. Shown are (a) the electrical resistivity $\rho(T)$, (b) the thermal conductivity $\kappa(T)$, and (c) the calculated and experimental Seebeck coefficient $S(T)$.

regular metallic behavior. The inset shows the resistivity as a function of temperature on a logarithmic scale. Below 50 K the resistivity becomes 0.27 $\mu\Omega$ m, nearly independent of temperature, while above this value the resistance increases with increasing temperature. The temperature-independent part at low temperatures was suggested to be typical for half-metallic ferromagnets.[51,52] The residual resistivity ratio is $R_{RR} = \rho(300\text{ K})/\rho(2\text{ K}) = 1.8$. This value is small compared to other polycrystalline Heusler compounds. The overall low values of the resistivity are also remarkable, being a factor of 100 smaller compared to those of polycrystalline Co_2MnSi samples that were produced in the same way (from data not shown here). Both together point to the high quality of the Co_2MnGe samples.

Figure 15(b) shows the temperature-dependent thermal conductivity $\kappa(T)$ of Co_2MnGe. At low temperatures, $\kappa(T)$ increases with a T^3 law and a maximum appears between 40 and 50 K. Above 100 K, $\kappa(T)$ increases linearly with temperature. This behavior arises from the large electronic component of the total thermal conductivity in metals.[53]

The Seebeck coefficient $S(T)$ [see Fig. 15(c)] is negative in the entire temperature range. Similar to $\rho(T)$, the absolute value is almost constant below 50 K, as shown using a logarithmic scale in the inset of Fig. 15(c), and increases with increasing temperature. The value of -17μV K^{-1} at 300 K is comparable to that of elemental metals Co (-30.8 μV K^{-1}) and Mn (-9.8 μV K^{-1}). Similar values are observed in other polycrystalline Heusler compounds.[54] $S(T)$ was calculated from the electronic structure using a modified version[55] of

BOLTZTRAP[56] and compared to the experiment as shown in Fig. 15(c). The measured value agrees well with the calculated one. Deviations are seen at low temperatures where one expects the largest influence of the phonon-drag effect at about 0.2 times the Debye temperature,[57] which here is at about 80 K. At elevated temperatures the electronic structure starts to deviate from that of the ground-state half-metallic ferromagnet and minority and majority states start to mix owing to the thermal fluctuations already below the Curie temperature. This explains the deviations between measured and calculated $S(T)$ at higher temperatures.

IV. SUMMARY

In summary, the structural, electronic, magnetic, mechanical, and transport properties of the half-metallic ferromagnet Co_2MnGe have been studied in detail. The crystalline structure of Co_2MnGe was investigated by XRD, EXAFS, and anomalous XRD and it was found that the compound exhibits the $L2_1$ structure typical for well-ordered Heusler compounds. The vibrational and mechanical properties of the compound were calculated. The comparison of observed and calculated mechanical properties proves a covalent-like bonding of Co_2MnGe. Band-structure calculations based on the $L2_1$ structure result in a half-metallic ferromagnetic ground state for the compound. The compound is a localized magnetic moment system with a ground-state magnetic moment of $5\mu_B$ in the primitive cell. This is in excellent agreement to the SQUID measurement, which revealed a magnetic moment of $4.982\mu_B$ at 5 K. Thus, Co_2MnGe fulfills the requirement for half-metallicity according to the Slater-Pauling rule. The transport measurements show the expected metallic behavior with a resistivity of 0.48 $\mu\Omega$ m and a Seebeck coefficient of -16μV K^{-1} at room temperature. The temperature independence of the resistivity below 50 K supports the occurrence of half-metallic ferromagnetism in this compound. The bulk sensitivity of HAXPES was used to explore the core levels as well as the valence-band electronic structure of polycrystalline Co_2MnGe. The measured valence-band spectra are clearly resolved and in good agreement with the first-principles calculations of the electronic structure. Spin-orbit splitting and exchange splitting of the core levels are explored in detail. Multiplet calculations of $2p$ and $3s$ core levels were performed for Mn in 2+ and 3+ ionic states to determine the importance of the many- electron contributions to the core-level photoelectron spectra of the compound. Comparison of the calculation to the experiment revealed that the state of Mn cannot be identified as being a definite ionic one.

ACKNOWLEDGMENTS

This work was financially supported by the Deutsche Forschungs Gemeinschaft (DfG) (projects no. TP 1.2-A and TP 1.3-A of Research Unit FOR 1464 ASPIMATT) and DfG-JST (project no. FE633/6-1). The authors thank the staff of the LNLS (Campinas, Brazil) for support as well as Fabio Furlan Ferreira and Gustavo Azevedo (LNLS, Campinas) for help with the XRD and EXAFS experiments. Support of this work was provided by the Brazilian Synchrotron Light Laboratory (LNLS) under proposals D10B-XPD-6689 and D04B-XAFS1-6699. The HAXPES measurements were performed at BL47XU of SPring-8 (Hyogo, Japan) with the approval of the Japan Synchrotron Radiation Research Institute (JASRI) (Long-term Proposal 2008B0017) and at BL15XU of SPring-8 with the approval of NIMS (Nanonet Support Proposal 2008B4903). The authors are grateful to HiSOR, Hiroshima University, and JAEA/Spring-8 for the development of HAXPES at BL15XU of Spring-8. This work was partially supported by the Nanotechnology Network Project, MEXT, Japan.

*fecher@uni-mainz.de

[1] C. Felser, G. H. Fecher, and B. Balke, Angew. Chem., Int. Ed. Engl. **46**, 668 (2007).
[2] T. Graf, C. Felser, and S. S. P. Parkin, Prog. Solid State Chem. **39**, 1 (2011).
[3] R. A. de Groot, F. M. Müller, P. G. van Engen, and K. H. J. Buschow, Phys. Rev. Lett. **50**, 2024 (1983).
[4] J. Kübler, A. R. Williams, and C. B. Sommers, Phys. Rev. B **28**, 1745 (1983).
[5] P. Webster, J. Phys. Chem. Solids **32**, 1221 (1971).
[6] T. Ambrose, J. Krebs, and G. Prinz, Appl. Phys. Lett. **76**, 3280 (2000).
[7] T. Ishikawa, T. Marukame, K. i. Matsuda, T. Uemura, M. Arita, and M. Yamamoto, J. Appl. Phys. **99**, 08J110 (2006).
[8] S. Hakamata, T. Ishikawa, T. Marukame, K. i. Matsuda, T. Uemura, M. Arita, and M. Yamamoto, J. Appl. Phys. **101**, 09J513 (2007).
[9] F. F. Ferreira, E. Granado, W. Carvalho, S. W. Kycia, D. Bruno, and R. Droppa, J. Synchrotron Radiat. **13**, 46 (2006).
[10] H. C. N. Tolentino, A. Y. Ramos, M. C. M. Alves, R. A. Barrea, E. Tamura, J. C. Cezar, and N. Watanabe, J. Synchrotron Radiat. **8**, 1040 (2001).
[11] S. Ueda, Y. Katsuya, M. Tanaka, H. Yoshikawa, Y. Yamashita, S. Ishimaru, Y. Matsushita, and K. Kobayashi, AIP Conf. Proc. **1234**, 403 (2010).
[12] D. T. Cromer, J. Appl. Cryst. **16**, 437 (1983).
[13] W. Kraus and G. Nolze, J. Appl. Cryst. **29**, 301 (1996).
[14] J. Laugier and B. Bochu [http://www.ccp14.ac.uk/tutorial/lmgp/scatfac.htm].
[15] D. Koningsberger and R. Prins, *X-ray Absorption: Principles, applications and techniques of EXAFS, SEXAFS and XANES in Chemical Analysis, Chemical Analysis*, Vol. 92 (John Wiley & Sons, New York, 1988).
[16] M. Newville, J. Synchrotron Radiat. **8**, 322 (2001).
[17] S. I. Zabinsky, J. J. Rehr, A. Ankudinov, R. C. Albers, and M. J. Eller, Phys. Rev. B **52**, 2995 (1995).
[18] P. Blaha, K. Schwarz, G. K. H. Madsen, D. Kvasnicka, and J. Luitz, *WIEN2k, An Augmented Plane Wave + Local Orbitals Program for Calculating Crystal Properties* (Technische Universitt Wien, Wien, Austria, 2001).
[19] H. C. Kandpal, G. H. Fecher, and C. Felser, J. Phys. D **40**, 1507 (2007).

[20]J. P. Perdew, K. Burke, and M. Ernzerhof, Phys. Rev. Lett. **77**, 3865 (1996).
[21]I. Galanakis, P. Dederichs, and N. Papanikolaou, Phys. Rev. B **66**, 174429 (2002).
[22]G. H. Fecher, H. C. Kandpal, S. Wurmehl, C. Felser, and G. Schönhense, J. Appl. Phys. **99**, 08J106 (2006).
[23]K. Miyamoto, K. Iori, A. Kimura, T. Xie, M. Taniguchi, S. Qiao, and K. Tsuchiya, Solid State Commun. **128**, 163 (2003).
[24]K. Miyamoto, A. Kimura, K. Iori, K. Sakamoto, T. Xie, T. Moko, S. Qiao, M. Taniguchi, and K. Tsuchiya, J. Phys. Condens. Matter **16**, 5797 (2004).
[25]V. N. Antonov, O. Jepsen, A. N. Yaresko, and A. P. Shpak, J. Appl. Phys. **100**, 043711 (2006).
[26]P. Klaer, T. Bos, M. Kallmayer, C. G. F. Blum, T. Graf, J. Barth, B. Balke, G. H. Fecher, C. Felser, and H. J. Elmers, Phys. Rev. B **82**, 104410 (2010).
[27]S. Ouardi, B. Balke, A. Gloskovskii, G. H. Fecher, C. Felser, G. Schönhense, T. Ishikawa, T. Uemura, M. Yamamoto, H. Sukegawa, W. Wang, K. Inomata, Y. Yamashita, H. Yoshikawa, S. Ueda, and K. Kobayashi, J Phys. D **42**, 084010 (2009).
[28]C. S. Fadley and D. A. Shirly, Phys. Rev. A **2**, 1109 (1970).
[29]R. D. Cowan, *The Theory of Atomic Structure and Spectra* (University of California Press, Berkeley, 1981).
[30]G. van der Laan, J. Phys. Condens. Matter **3**, 7443 (1991).
[31]F. de Groot, Coordin. Chem. Rev. **249**, 31 (2005).
[32]F. de Groot and A. Kotani, *Core Level Spectroscopy of Solids* (CRC Press, Boca Raton, FL, 2008).
[33]P. S. Bagus, R. Broer, W. A. de Jong, W. C. Nieuwpoort, F. Parmigiani, and L. Sangaletti, Phys. Rev. Lett. **84**, 2259 (2000).
[34]E. Stavitski and F. M. F. de Groot, Micronesica **41**, 687 (2010).
[35]K. Kobayashi, Nucl. Instrum. Methods Phys. Res. A **601**, 32 (2009).
[36]R. G. Cavell, S. P. Kowalczyk, L. Ley, R. A. Pollak, B. Mills, D. A. Shirley, and W. Perry, Phys. Rev. B **7**, 5313 (1973).
[37]P. S. Wehner, J. Stöhr, G. Apai, F. R. Mc Feely, R. S. Williams, and D. A. Shirley, Phys. Rev. B **14**, 2411 (1976).
[38]F. D. Murnaghan, Proc. Natl. Acad. Sci. USA **30**, 244 (1944).
[39]F. Birch, J. Geophys. Res. **57**, 227 (1952).
[40]M. Born and K. Huang, *Dynamical Theory of Crystal Lattices* (Clarendon Press, Oxford, 1956).
[41]J. F. Nye, *Physical Properties of Crystals* (Oxford Science Publications, Oxford, 1985).
[42]J. Wang, S. Yip, S. R. Phillpot, and D. Wolf, Phys. Rev. Lett. **71**, 4182 (1993).
[43]O. L. Anderson, J. Phys. Chem. Solids **24**, 909 (1963).
[44]G. Chin, Trans. Amer. Crystallographic Assoc. **11**, 1 (1975).
[45]J. J. Gilman, *Hardness - A Strength Microprobe*, Chapter 4 in The Science of Hardness Testing and Its Research Applications, edited by J. H. Westbrook and H. Conrad, (American Society of Metals, Metals Park, Ohio, USA, 1973), p. 65.
[46]J. J. Gilman, *Chemistry and Physics of Mechanical Hardness* (Wiley, Hoboken, NJ, 2009).
[47]D. Tabor, *The Hardness of Metals* (Clarendon Press, Oxford, 1951).
[48]K. Parlinski, Z-Q. Li, and Y. Kawazoe, Phys. Rev. Lett. **78**, 4063 (1997).
[49]J. L. F. Fraga, D. E. Brandao, and J. G. Sereni, J. Magn. Magn. Mater. **102**, 199 (1991).
[50]E. Sevillano, H. Meuth, and J. J. Rehr, Phys. Rev. B **20**, 4908 (1979).
[51]M. J. Otto, R. A. M. van Woerden, P. J. van der Valk, J. Wijngaard, C. van Bruggen, and C. Haas, J. Phys. Condens. Matter **1**, 2351 (1989).
[52]C. G. F. Blum, C. A. Jenkins, J. Barth, C. Felser, S. Wurmehl, G. Friemel, C. Hess, G. Behr, B. Büchner, A. Reller, S. Riegg, S. G. Ebbinghaus, T. Ellis, P. J. Jacobs, J. T. Kohlhepp, and H. J. M. Swagten, Appl. Phys. Lett. **95**, 161903 (2009).
[53]D. M. Rowe, *Thermoelectrics Handbook: Macro to Nano*, 1st ed. (CRC/Taylor & Francis, Boca Raton, FL, 2006).
[54]B. Balke, S. Ouardi, T. Graf, J. Barth, C. G. F. Blum, G. H. Fecher, A. Shkabko, A. Weidenkaff, and C. Felser, Solid State Commun. **150**, 529 (2010).
[55]J. Barth, G. H. Fecher, B. Balke, S. Ouardi, T. Graf, C. Felser, A. Shkabko, A. Weidenkaff, P. Klaer, H. J. Elmers, H. Yoshikawa, S. Ueda, and K. Kobayashi, Phys. Rev. B **81**, 064404 (2010).
[56]G. K. H. Madsen and D. J. Singh, Comput. Phys. Commun. **175**, 67 (2006).
[57]J. M. Ziman, Electrons and Phonons (Oxford University Press, Oxford, 1960).